Supplementary Information for

Electrochemically-enhanced nuclear fusion of deuterium

Kuo-Yi Chen[1], Phil A. Schauer[1], Sergey Issinski[1], Fatima H. Garcia[1], Ryan Oldford[1], Luca Egoriti[2], Shota Higashino[1], Jannis Maiwald[1], Aref E. Vakili[1], Yunzhou Wen[1], Joseph Koh[1], Thomas Schenkel[3], Monika Stolar[1], Amanda K. Brown[1], and Curtis P. Berlinguette* [1,4,5,6]

[1]Department of Chemistry, The University of British Columbia, 2036 Main Mall, Vancouver, British Columbia, Canada

[2]TRIUMF, 4004 Wesbrook Mall, Vancouver, British Columbia, Canada

[3]Accelerator Technology and Applied Physics Division, Lawrence Berkeley National Laboratory, Berkeley, CA, USA

[4]Department of Chemical and Biological Engineering, The University of British Columbia, 2360 East Mall, Vancouver, British Columbia, Canada

[5]Stewart Blusson Quantum Matter Institute, The University of British Columbia, 2355 East Mall, Vancouver, British Columbia, Canada

[6]Canadian Institute for Advanced Research (CIFAR), 661 University Avenue, Toronto, Ontario, Canada

*Corresponding author: Curtis P. Berlinguette (cberling@chem.ubc.ca)

Supplementary Note 1: Fuel density in palladium deuteride

We calculated the fuel density in palladium deuteride (PdD) using the formula:

$$\rho_D = \frac{Z}{V}$$

where Z is the number of formula units per unit cell and V is the volume of the unit cell.

The fuel density of palladium deuteride, with a D:Pd ratio of 1, a unit cell volume of 68.12 $Å^3$ (68.12×10^{-30} m^3), and 4 D atoms per unit cell at 77 K is calculated as[1]:

$$\rho_D = \frac{4}{68.12\times10^{-30}\, m^3} = 5.9\times10^{28}\, m^{-3}$$

Supplementary Note 2: Mean free path in the Thunderbird Reactor

The mean free path (λ) of deuterium gas can be estimated using the following equation[4]:

$$\lambda = \left(\frac{k_B T}{\sqrt{2}\pi d^2 p}\right)$$

where k_B is Boltzmann constant, T is the temperature of the residual deuterium gas in the chamber, d is the kinetic diameter of a deuterium gas, and p is the pressure in the vacuum chamber.

We assumed the kinetic diameter of deuterium gas to be 289 pm [5], the temperature of the residual deuterium gas to be equivalent to the gas inlet temperature of 300 K, and a maximum pressure in the Thunderbird Reactor of 4×10^{-5} *Torr* (5.3×10^{-3} *Pa*). This results in a mean free path of the deuterium gas of:

$$\lambda = \frac{(1.38\times10^{-23}\,JK^{-1})(300\,K)}{\sqrt{2}\pi(289\times10^{-12}\,m)^2(5.3\times10^{-3}\,J/m^3)} = 2.1\,m$$

The kinetic diameter of deuterium ions and electrons is smaller than that of deuterium gas[6], therefore we defined the mean free path of 2.1 m as the lower bound of the mean free path.

The value of the mean free path is 30 times greater than the distance between the palladium target and the thruster outlet (6.8 cm; Supplementary Fig. 1), indicating that deuterium ions can travel unimpeded through the chamber to the target. Based on this, we assumed that any rate of fusion events in the plasma phase are negligible.

Supplementary Note 3: Reactor control software

We designed a custom reactor control and data acquisition system comprising device monitors connected to a central server via WiFi. The device monitors (e.g. Arduino MKR-1010 WiFi, Raspberry Pi Zero) were paired with reactor devices, including current meters, a mass flow controller, and a microwave generator. These monitors managed communication and data acquisition for the attached devices, ensuring synchronization using Coordinated Universal Time (UTC) for precise timestamping.

The central server operated with a Mosquitto MQTT server, a Redis database, a custom backend developed in Python/Flask, and frontend developed in NodeJS, React, and Redux, ensuring efficient management of reactor operations and data acquisition.

Supplementary Note 4: Comparison of a palladium member reactor to Thunderbird Reactor

Inspired by previous work, we modified a palladium membrane reactor, originally designed for electrochemically-driven hydrogenation, to couple with the vacuum chamber at the core of the Thunderbird Reactor. In short, in the palladium membrane reactor, electrolysis occurs in a 1 M $H_2SO_{4(aq)}$ solution. Protons (H^+) generated from electrolysis are reduced to hydrogen atoms (H) at the palladium membrane, which also acts as the cathode. The H pass through the palladium membrane into the hydrogenation chamber, where they hydrogenate an unsaturated chemical bond. In the Thunderbird Reactor, electrolysis occurs in a 2 M K_2CO_3 solution in D_2O. The D_2O is then reduced to deuterium atoms (D) at the palladium target, which acts as a cathode. The D are absorbed into the palladium target, where they potentially fuse with D sourced from the ion source. A schematic comparing the two reactors is provided in Supplementary Fig. 2.

Supplementary Note 5: Neutron detection and analysis

Neutron detector

Fusion rates were observed using a single-detector neutron counting system, referred to as the “EJ-309 detector”. The EJ-309 detector consists of a 12.7 × 12.7 cm cylindrical cell from Eljen (model: 510-50×50-9) filled with an liquid scintillator (EJ-309) and coupled with a Hamamatsu R1250 photomultiplier tube (PMT) encased in a Mu-metal shield (Supplementary Fig. 3).

The PMT was biased by a CAEN R1470ET high voltage power supply. The output signal from the PMT was directly sampled and digitized with a 14-bit 500 MHz CAEN DT5730S waveform digitizer equipped with DPP-PSD firmware. The digitizer’s performance was optimized by aligning the expected leading edge of 2.45 MeV neutrons with the center of its dynamic range. This was achieved by setting the PMT bias voltage to –1,525 V. The neutron data were collected using CAEN CoMPASS software[7].

Detector response to neutrons and gamma rays

The EJ-309 scintillator is filled with scintillation liquid (Eljen Technology; NEUTRON/GAMMA PSD EJ-309), which is excited when a particle interacts with the molecules of the liquid. This excitation results in molecules that are either hot (vibrational excitation) and/or excited (electronic excitation). When these molecules relax to a ground state, photons in the visible spectrum are emitted by photoluminescence at around 10^{-9} s. The amount of light produced, known as the light output, is measured in keVee (kilo-electron volts equivalent). The light output is proportional to the type of incident particle and the amount of energy deposited into the scintillator. The amount of light produced by a 1 MeV gamma ray differs from that produced by a 1 MeV neutron due to the distinct interaction mechanics with the liquid. Gamma rays primarily deposit their energy in the detector through Compton scattering because the EJ-309 scintillator is composed of low atomic number elements like carbon and hydrogen. On the other hand, neutrons (1–5 MeV) deposit energy mainly through elastic scattering with hydrogen and, to a lesser extent, with carbon nuclei[8]. These different interactions result in a characteristic pulse height spectrum, referred to as the gamma-ray response and the neutron response (Supplementary Fig. 4)[9].

Electric noise mitigation

Electrical noise was minimized by matching impedances between the PMT and the digitizer. An RG316 coaxial cable (length: 1.83 m; purchased from CD International Technology) was used between the detector and the digitizer. The remaining noise floor was removed by setting the signal amplitude threshold in the CoMPASS software to 250 least significant bits, which corresponds to 50 keVee.

Pileup rejection

If two or more particles hit the detector at the same time, they can cause a pileup of multiple signals in a single acquisition window. The contribution from these pileup events was kept <2% of the total neutron count rate by setting the pileup rejection threshold in CoMPASS to 17 keVee and positioning the detector approximately 12 cm from the target.

Magnetic shielding

The magnetic field generated by the permanent magnets in the thruster significantly interferes with the PMT of the EJ-309 detector. This magnetic field deflects the trajectories of the photoelectrons and electrons within the PMT region, resulting in poor detection efficiency and a degraded pulse height spectrum. The strength of the magnetic field was reduced from 40 Gauss to <0.3 Gauss at the front of the detector by installing a double-layer magnetic shield manufactured from Mu-metal and Co-NETIC (Supplementary Fig. 3). The external layer of the shield is 57.6 cm long and has a radius of 10.54 cm, the internal layer is 55.1 cm long and has a radius of 9.30 cm.

The effectiveness of the shielding was experimentally verified by comparing the Compton edge position of the ^{40}K isotope with the literature value. The Compton edge (L; measured in keVee) is calculated by:

$$L = 2\left(\frac{E_{\gamma}^{2}}{2E_{\gamma} + 511}\right)$$

where E_{γ} is the energy of the incident gamma-ray photon measured in keV and 511 keV is the rest energy mass of the electron.

The position of the Compton edge was determined by taking the first derivative of the detector response function as described by Safari[10]. The literature gamma-ray energy peak of ^{40}K was precisely measured to be 1,461 keV[11]. This value can be converted to a Compton edge by:

$$L = 2\left(\frac{(1{,}461\ keV)^{2}}{2(1461\ keV) + 511\ keV}\right) = 1,243\ keVee$$

Our measured Compton edge of 1,270 keVee is less than 3% of the calculated Compton edge of ^{40}K, 1243 keVee.

Particle discrimination

The EJ-309 detector is capable of detecting both neutrons and gamma rays. The two types of radiation were distinguished from each other by charge integration. Charge integration is a pulse shape discrimination technique that uses the different scintillation decay times in the EJ-309 detector[12]. The decay time for gamma-ray interactions is faster than neutron interactions [13]. A pulse shape discrimination (PSD; Supplementary Fig. 4) variable was constructed by calculating the ratio of the integrals of the "tail" and "total" gates. The tail gate refers to a portion of the decay of the pulse after the pulse peak, while the total gate encompasses the entire pulse (Supplementary Fig. 4)[14,15].

Counting window construction

A neutron counting window (Supplementary Fig. 4) was constructed in the following way:

The PSD plot was cut into slices of an equal width of 5 keVee. The gamma-ray peak was then fit using a Gaussian distribution to determine its mean, μ, and standard deviation, σ (Supplementary Fig. 4).

a. The lower PSD boundary of the counting window was then set as $\mu + 5\sigma$, similar to the method used by Baramsai *et al.*[16].
b. The upper boundary was defined by adding an arbitrary 0.2 PSD units to the lower boundary.
c. The left boundary was fixed at 50 keVee, using the lower energy threshold set in the CoMPASS software.

Neutron Energy Estimation

The energy of the counted neutrons was estimated through a two-step process:
First, a calibration curve was built to convert the measured signal into light output of the EJ-309 liquid scintillator by using ^{60}Co, ^{137}Cs, and ^{152}Eu gamma-ray radioactive sources (Supplementary Fig. 5)[17].

Second, the experimental neutron response was compared with the simulated response generated using the Monte Carlo N-Particle (MCNP6.2) transport code[18]. The simulation specifically modeled the energy deposition within the EJ-309 scintillation liquid. A point source with a peak energy of 2.45 MeV, representative of neutrons produced in D-D fusion, was simulated using a Gaussian energy distribution with a standard deviation of 0.5 MeV to accurately model the characteristics of a physical source that emits 2.45 MeV neutrons[19]. The source was positioned 0.12 m from the front surface of the EJ-309 scintillator, following the methodology of Bai *et al.*[20]. The resolution of the detector was accounted for by incorporating a resolution function derived from Enqvist *et al.*[9].

The Detector Response Function Toolkit (DRiFT) toolkit[21] was utilized alongside MCNP6.2 to convert the simulated energy deposited by recoil protons in the scintillator (measured in keV) into a neutron response distribution (measured in keVee) (solid blue line in Supplementary Fig. 6). The comparison of the experimentally observed and simulated neutron responses demonstrates a reasonable agreement, with overlapping and matching trends in the response functions from 200 to 1000 keVee (Supplementary Fig. 6). The simulated responses were scaled to match the measurements by normalizing to the maximum count in the measured spectra. The discrepancy observed below 200 keVee is attributed to the experimental cutoff at 50 keVee, truncating part of the neutron spectrum. The simulation was performed using 10^7

neutrons, which provides sufficient statistics at energies up to 1000 keVee. Note that very few counts are experimentally observed beyond 1000 keVee. In order to produce the neutrons, the simulation would have to simulate many more interactions than those currently used.

Supplementary Note 6: Evidence for lattice confinement fusion

An experiment to test whether the fusion events were occurring inside the lattice rather than in the gas phase was conducted by cycling the sheath voltage (Supplementary Fig. 7). The 'on' periods in this experiment were characterized by applying the sheath voltage (–30 kV) between the vacuum chamber and the target, accelerating D^+ ions into the target. During the 'off' periods, the sheath voltage was turned off, such that no more D^+ ions were implanted into the target. We began the experiment by using an annealed target, and performing a typical beam loading experiment (not shown), until the neutron production rates stabilized. Once stability was reached, we turned off the sheath voltage for 5 minutes, and then turned it back on for 10 minutes. This on-off cycle was repeated three times. At the first off period, we observed a decrease in the neutron production rate, returning to background levels (0.2 n/s). At the first 'on' period, we observed an immediate increase in the neutron production rate, stabilizing at 184.1(7) n/s, rather than the gradual increase expected at the beginning of a typical beam loading cycle. The same behavior was noted in the subsequent on-off cycles. The result indicates that the concentration of deuterium in the Pd target reached a saturation value during the first beam loading instance, and the concentration remained constant as the beam loading cycles were repeated.

In-situ XRD experiments (see Supplementary Methods, *In situ XRD characterization of palladium targets*) validate that the deuterium remains in the metal lattice for a prolonged period of time, indicating there is negligible loss of deuterium in the Pd target while the sheath voltage is turned off. This demonstrates that after reapplying the sheath voltage, deuterium does not need to accumulate in the Pd metal lattice again; it can fuse with the deuterium already present in the Pd target. This is evidence that high-energy deuterium ions collide with deuterium within the Pd lattice, triggering D-D fusion rather than fusion reactions occurring with deuterium in the gas phase.

Supplementary Note 7: Fusion energy gain factor Q of the Thunderbird Reactor

The fusion yield Y of the Thunderbird Reactor can be estimated using the formula:

$$Y = 2N \frac{4\pi}{\varepsilon_{in}\,\Omega}$$

where 4π is the total solid angle of a sphere (in steradians), N is the number of detected neutrons, ε_{in} is the intrinsic efficiency of the detector, and Ω is the solid angle covered by the detector (in steradians). The factor of 2 accounts for our measurement of only one of the two equally probable D-D fusion pathways, as our experiment detects only neutrons, which represent half of the total fusion yield.

We assumed a point source in front of a right circular cylindrical detector:

$$\Omega = 2\pi(1 - \frac{d}{\sqrt{d^2+r^2}})$$

where d is the source-detector distance and r the detector radius[2].

At a source distance of 0.12 m from the detector and a detector radius 0.0635 m, the solid angle is:

$$\Omega = 2\pi(1 - \frac{0.12m}{\sqrt{(0.12\,m)^2+(0.0635\,m)^2}}) = 0.73\,sr$$

The intrinsic efficiency of our detector is 54% [3]. At a sheath voltage of −30 kV and a plasma current of 0.5 mA we detected a maximum neutron rate of $N = 165\,neutrons/s$, which results in a fusion yield of:

$$Y = 2 \times 165\,neutrons/s \;\; \frac{12.57\,sr}{0.54 \times 0.73\,sr} = 10523\,events/s$$

We calculated the average energy per each D-D fusion reaction:

$$E_{reac}(J) = E_{reac}(MeV) \cdot C_{eV-J}$$

where $E_{reac}(MeV)$ is the average energy per D-D fusion reaction in units of megaelectronvolts and C_{eV-J} is the conversion factor from electronvolt to Joule ($1.6{\times}10^{-19}\frac{J}{eV}$).

The average energy released per each D-D fusion reaction is $3.65\,MeV$:

$$E_{reac} = (3.65\,MeV)(1.6\times10^{-19}\frac{J}{eV}) = 5.84\times10^{-13}J$$

The total power output P_{out} of the reactor is calculated as:

$$P_{out} = Y \cdot E_{reac}$$

$$P_{out} = (10523\,s^{-1})(5.84\times10^{-13}J) = 6.15\times10^{-9}\,\frac{J}{s}.$$

The power input of the reactor is calculated as:

$$P_{in} = V_S \cdot I_P$$

where V_S is the sheath voltage and I_S is the plasma current.

$$P_{in} = (30\,kV)(0.5\,mA) = 15\,\frac{J}{s}$$

The fusion gain factor Q is obtained as:

$$Q = \frac{P_{out}}{P_{in}}$$

$$Q = \frac{6.15\times10^{-9}\,\frac{J}{s}}{15\,\frac{J}{s}} = 4.1\times10^{-10}$$

Supplementary Methods

Palladium target/cathode preparation

The palladium target was rolled from a palladium bar (100 g, 99.95% purity, purchased from Valcambi). The bar was first manually cold-rolled to <500 µm using a Pepetools 90 mm Flat Rolling Mill, and then automatically cold-rolled to a final thickness of 300 µm using an MTI EQ-MR100A Electric Rolling Press. The final thickness was measured with a Mitutoyo digital micrometer to an accuracy of ± 1 µm. Targets were cut from the 300 µm palladium sheet into a disc shape with a diameter of 2.4 cm using a die cutter. The disk-shaped targets were cleaned with deionized water and annealed at 400 °C for one hour at 10^{-5} Torr in a 50 mm quartz vacuum tube installed in a MTI OTF-1200X-S tube furnace. After annealing, the targets were polished with a sandpaper (CW 1200) and washed with isopropyl alcohol using a kim wipe before use in the reactor. The annealing and cleaning procedures were performed between each fusion experiment to remove deuterium from the palladium. The targets were characterized with X-ray diffraction (XRD) to confirm the absence of deuterium from the palladium lattice.

The annealing procedure was based on Sieverts' law. According to Holleck[22], the relationship between the hydrogen concentration in metals and hydrogen gas pressure is given by:

$$\left(\frac{P_{H2}}{P_0}\right)^{1/2} = K(T)n,$$

where P_{H2} is the partial pressure of hydrogen, $P_0 = 1$ Torr, $K(T)$ is Sieverts' constant at a specified temperature (e.g., 2.1×10^3 at 400 °C) and n is the molar ratio of hydrogen in the metal.

We assumed the volume fraction of hydrogen gas in the vacuum chamber to be the same as that in ambient air, 5×10^{-5} vol% [23], which results in $P_{\mathrm{H2}} = 5.0\times10^{-12}$ Torr for the total pressure of 10^{-5} Torr in the vacuum tube furnace. Thus, the molar ratio of hydrogen (n) at 400 °C is:

$$n = \left(\frac{5\times10^{-12}\,Torr}{1\,Torr}\right)^{1/2}/(2.1\times10^{3}) = 1.1\times10^{-9}$$

This low value of n suggests that the palladium targets will be completely deloaded by the annealing procedure described above.

X-ray diffraction (XRD) characterization of palladium targets

XRD spectra were collected on a Rigaku SmartLab X-ray diffractometer with Cu Kα radiation (1.5406 Å). A 2θ-omega scan for 20–90 degrees with a scan speed of 5 degrees/min and a step size of 0.05 degrees was performed using parallel beam optics. The XRD spectra of the Pd targets were collected at three different stages of the experiment: (i) prior to a fusion experiment, (ii) after a fusion experiment, and (iii) after annealing the target to remove deuterium from the palladium lattice. For each stage, XRD spectra were measured on both sides of Pd targets; the side exposed to the electrolyte in the electrochemical cell and the other exposed to the D^+ beam in the vacuum chamber. Prior to a fusion experiment, the Pd targets were scanned after the preparation method described above. After a fusion experiment, the Pd targets were scanned after they were removed from the Thunderbird Reactor and transferred to the XRD in ambient air within approximately 20 minutes. The Pd targets were scanned again after they were subsequently annealed at 400 °C for one hour at 10^{-5} Torr to remove deuterium from the Pd lattice.

Typical XRD spectra of Pd targets are shown in Supplementary Fig. 8. In this example, the fusion experiment included beam-loading for 60 min with a sheath voltage of −30 kV and a plasma current of 0.5 mA. This was followed by electrochemical loading for 60 min with a constant current of 200 mA across the electrochemical cell. Prior to fusion, the Pd target exhibited diffraction peaks for α-Pd (D/Pd < 0.01 [24]) phase both on the electrochemical cell and beam side (Supplementary Fig. 8). The lattice constants for the α-Pd phase prior to fusion were determined by Bragg's law for (111), (200), (220), and (311) peaks to be 3.894 ± 0.001 Å for the electrochemical cell side and 3.8941 ± 0.0006 Å for the beam side. These values are consistent with the 3.889 Å of pure palladium[25]. After fusion, the Pd target exhibited diffraction peaks for α-Pd and β-Pd (D/Pd > 0.6 [24]) on the electrochemical cell side and α-Pd on the beam side (Supplementary Fig. 8). Although we speculate that the absence of β-Pd on the beam side is attributed to the instability of deuterium in the Pd lattice at high temperature caused by the ion bombardment, we are currently do not have the infrastructure to provide direct evidence through *in situ* characterization of the Pd target in a beam-loading environment. The lattice constant of the α-Pd phase on the beam side was 3.896 ± 0.003 Å. After annealing, the Pd target exhibited α-Pd on both the electrochemical cell and beam sides, identical to the Pd target prior to the fusion experiment (Supplementary Fig. 8). The lattice constants for α-Pd after annealing were 3.8896 ± 0.0004 Å for the electrochemical side and 3.8925 ± 0.0004 Å for the beam side.

In situ XRD characterization of palladium targets

In situ XRD spectra were collected on a Rigaku SmartLab X-ray diffractometer with Cu Kα radiation (1.5406 Å) while the electrochemical cell was turned on. Two types of custom 3D-printed electrochemical cells fitted for *in situ* XRD measurements were used on the sample stage of the X-ray diffractometer. One cell exposed one side of the Pd target to ambient air while electrochemically loading the other side of the Pd target (Supplementary Fig. 9). The other one exposed one side of the Pd target to vacuum throughout the experiment while electrochemically loading the other side of the Pd target (Supplementary Fig. 10). These cells were designed in-house using SolidWorks computer aided design (CAD) software and 3D-printed using a Formlabs Form 3 stereolithography 3D printer with Formlabs clear resin (urethane dimethacrylate, methacrylate monomer and photoinitiator). The 200 mA constant current between the Pd target cathode and Ir wire anode was supplied by B&K Precision model 1550 switching DC bench power supply. All *in situ* XRD experiments were performed at room temperature (25 °C) with a 2 M K_2CO_3 solution in H_2O as an electrolyte.

We chose the Pd(H) (111) and (200) peaks located at $2\Theta = 40.1°$ and 46.6° for *in situ* XRD measurement. We performed looped scans from 35–50° with a scan speed of 5 degrees/min and a step size of 0.05 degree. For the electrochemical loading cycle, the DC power supply and XRD looped scans were initiated at the same time. The DC power supply was kept on at 200 mA for 60 min to load the Pd target, during which 17 scans of XRD measurements were performed. The voltage during the loading was approximately 12 V.

After the electrochemical loading cycle, we subsequently performed either a natural outgassing cycle in ambient air or under vacuum (10^{-2} Torr). To start the natural outgassing cycle, the DC power supply was turned off to keep the Pd target at its open circuit potential, while XRD looped scans were continuously performed for 18 hours.

In situ XRD spectra clearly showed the transition from α- to β-Pd phase during the electrochemical loading (Supplementary Fig. 11), which occurred in around 20 min after turning on the electrochemical cell. The resulting lattice constant of a β-Pd phase gives the H/Pd ratio by using Eq. 1 in[26], which is correlated to the D/Pd ratio of the Pd target in the Thunderbird Reactor. The electrochemical loading of more than 30 min yielded a single β-Pd phase. The H/Pd ratio achieved was typically around 0.7, indicating the formation of PdD with a high D/Pd ratio during the electrochemical loading in the Thunderbird Reactor (Supplementary Fig. 11).

The subsequent natural outgassing and vacuum cycles revealed that the β-Pd phase formed during the electrochemical loading cycle persisted over 18 hours, both in ambient air and in vacuum (Supplementary Fig. 12 and 13). The outgassing rate did not show a significant difference between in ambient air and under vacuum. The H/Pd ratio calculated from the lattice constant of the *β*-Pd(111) peak for the initial 60 min of the natural outgassing and vacuum cycle was higher than 0.6 for both cases, indicating that a *β*-Pd phase with a high H/Pd ratio was stable over the time scale of our fusion experiments with electrochemical loading cycled on and off.

Supplementary Figures

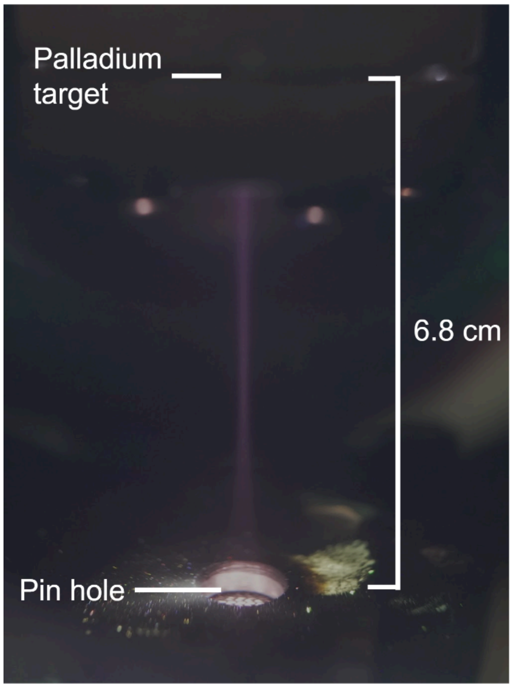

Supplementary Fig. 1: Pin hole placement in the Thunderbird Reactor. Plasma expelled from the plasma thruster below the pin hole travels upwards to the palladium target, where fusion events occur.

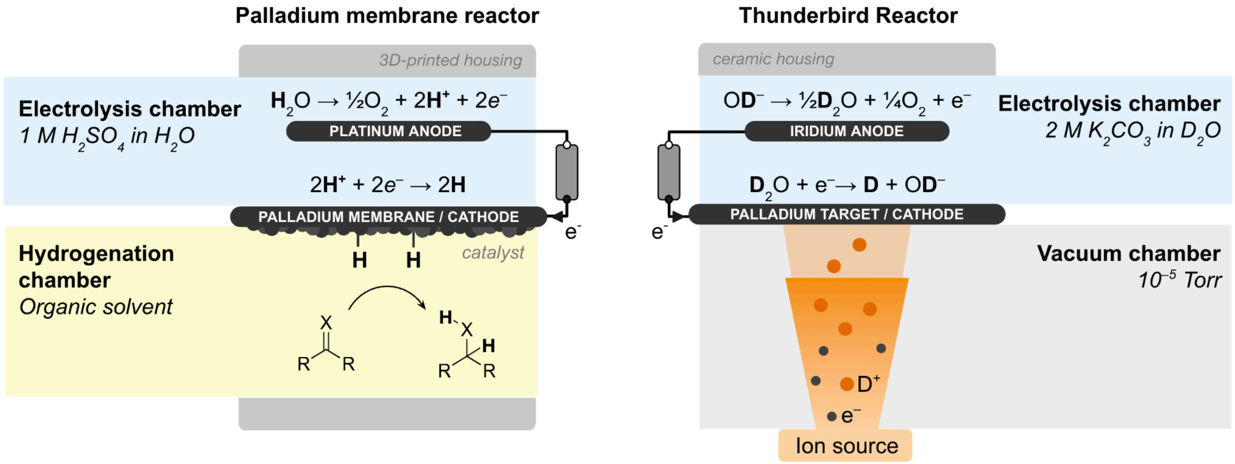

Supplementary Fig. 2: Illustrative comparison of a palladium membrane reactor and the Thunderbird Reactor. In the palladium membrane reactor, electrolysis occurs using a 1 M $H_2SO_{4(aq)}$ solution. Water is oxidized into protons (H^+) and oxygen gas ($O_{2(g)}$) at the platinum anode. The H^+ migrate to the palladium membrane where they are reduced to hydrogen atoms (H) at the palladium membrane, which also acts as the cathode. The H pass through the palladium membrane into the hydrogenation chamber, where they hydrogenate an unsaturated chemical bond. A high surface area catalyst on the palladium membrane, facing the hydrogenation chamber, facilitates the hydrogenation reaction. In the Thunderbird Reactor, electrolysis occurs in a 2 M K_2CO_3 solution in D_2O. Deuteroxide (OD^-) is oxidized into D_2O and $O_{2(g)}$ at the iridium anode. The D_2O is then reduced to deuterium atoms (D) at the palladium target, which acts as a cathode. The D are absorbed into the palladium target, where they potentially fuse with D sourced from the ion source.

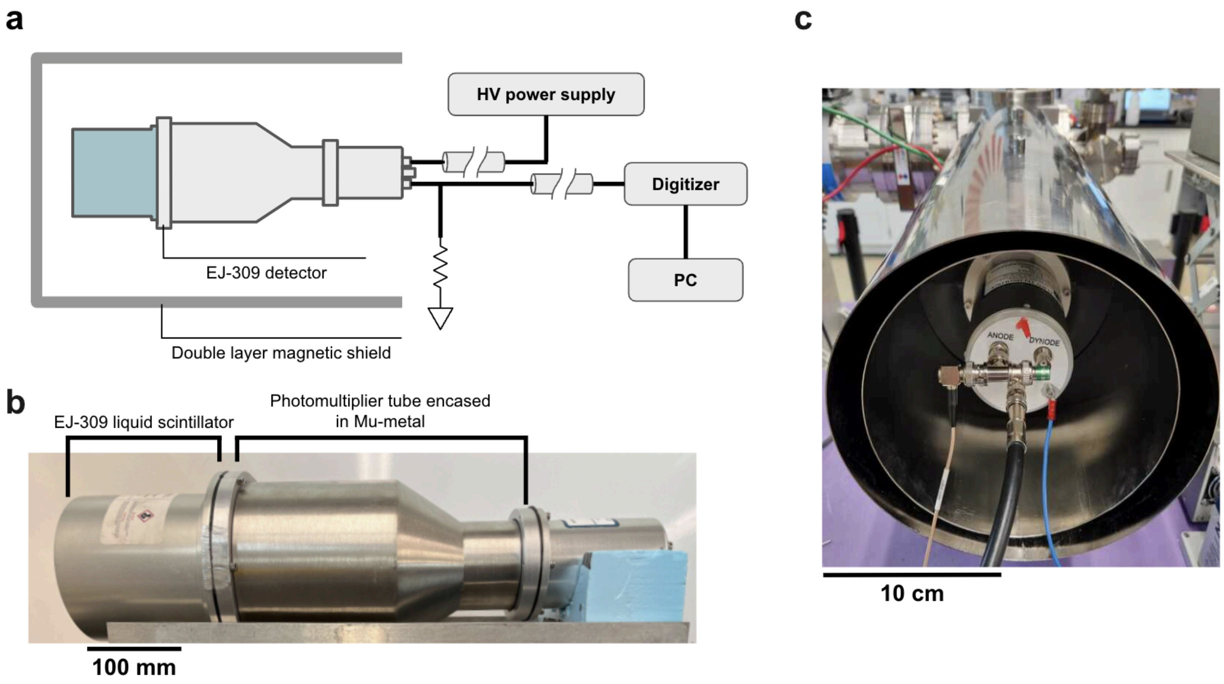

Supplementary Fig. 3: Neutron detector capabilities within the Thunderbird Reactor. a, : Schematic illustrating the neutron detection system as a part of the Thunderbird Reactor, highlighting key components of the system. **b,** A photo of the EJ-309 detector. **c**, EJ-309 detector, shown from the back, inside the double-walled magnetic shielding, composed of Mu-metal and Co-NETIC materials.

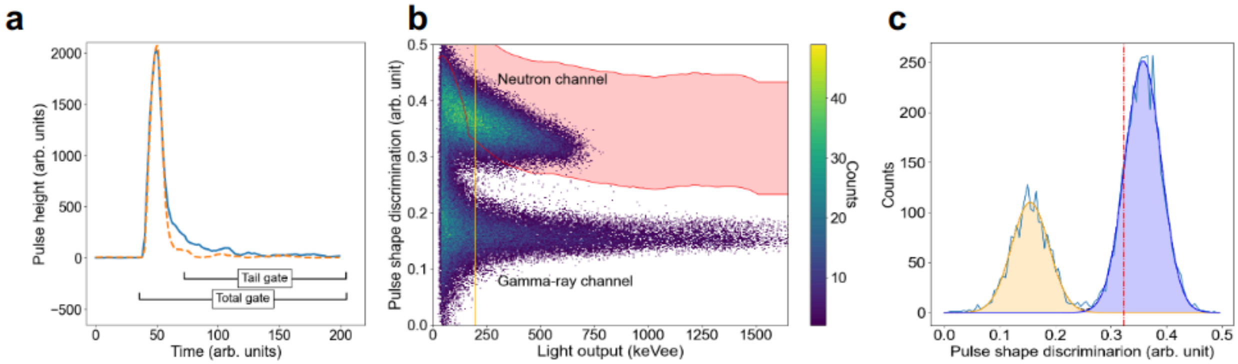

Supplementary Fig. 4: Particle discrimination within the Thunderbird Reactor. a, Sample waveforms, showing the difference between gamma-ray signals (dashed orange line), and neutrons (solid blue line). The “tail gate” refers to the portion of the waveform after pulse decay, while the “total gate” refers to the entire waveform. The ratio between the two is used to construct the pulse shape discrimination value. **b,** The result of neutron and gamma-ray discrimination. Red border outlines the neutron counting window. The vertical yellow line shows the location of a sample energy slice. **c,** Cross-section view of a sample energy slice, fit with two Gaussian distributions. The gamma-ray channel is in yellow and the neutron channel is in blue. The red dashed line indicates the 5σ cutoff from the gamma-ray distribution. The region to the right of this line will include only 0.00006% of detected gamma rays.

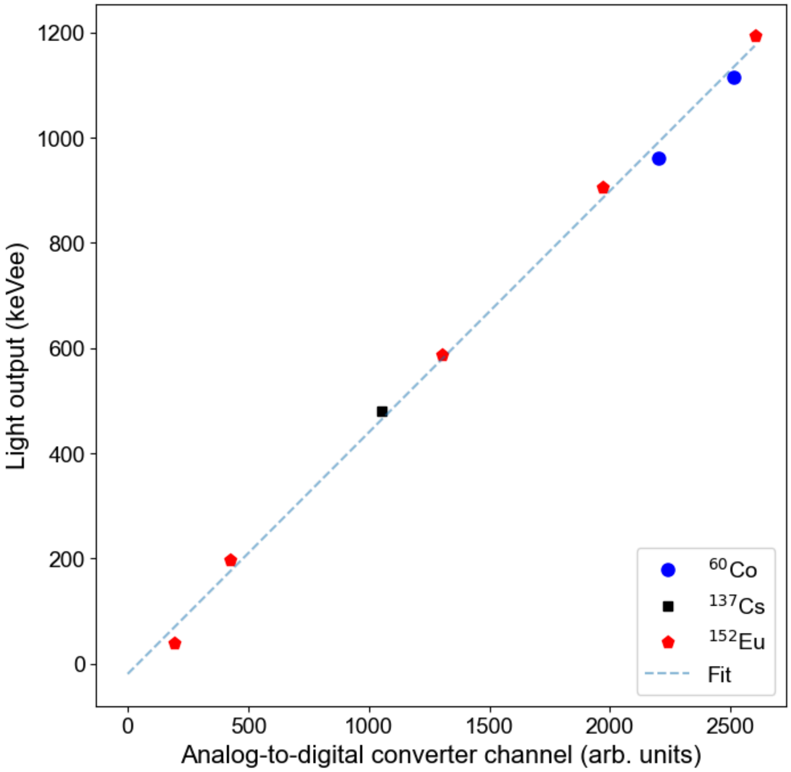

Supplementary Fig. 5: Energy calibration curve for the EJ-309 detector. The fit is linear (y = a $(x) + b$) with coefficients: $a = 2.179$, $b = 41.57$.

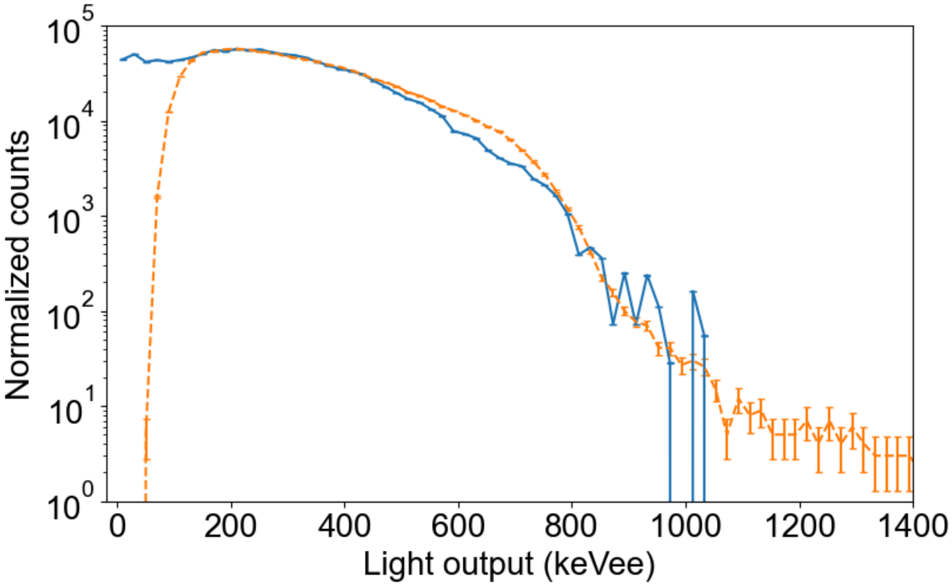

Supplementary Fig. 6: Neutron response for the EJ-309 detector exposed to 2.45 MeV neutrons from D-D fusion reactions. The measured data, obtained during an electrochemically-enhanced experiment, (dashed orange line) show good agreement with the simulated results (solid blue line), obtained using the Monte Carlo N-Particle (MCNP6.2) transport code. Error bars for the simulated data indicate the standard deviation from 10 simulation runs of 10^7 neutrons, while the error bars for the experimental data are calculated as the square root of the counts.

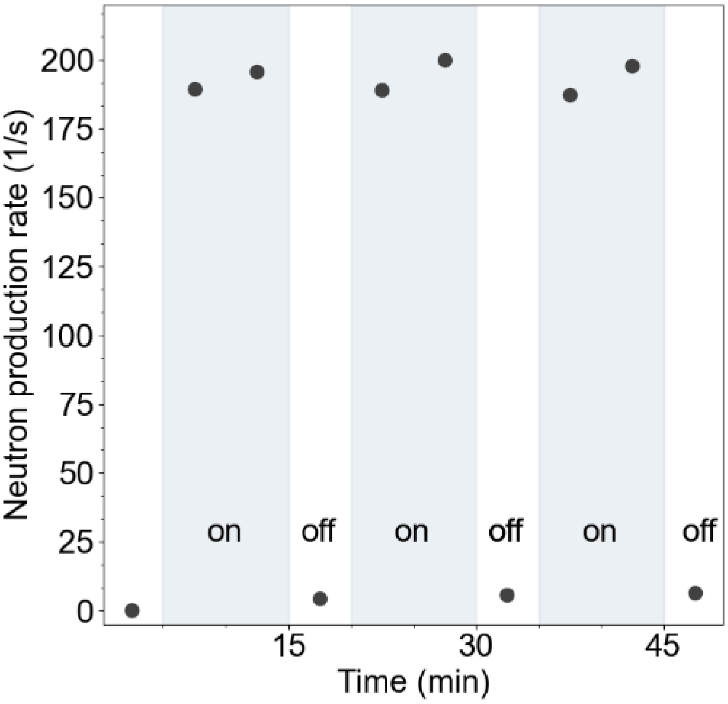

Supplementary Fig. 7: Experimental confirmation of lattice confinement fusion. Neutron production rates observed when sheath voltage of the reactor was cycled on and off during a beam-loading experiment. During the 10 min. "on" periods, the sheath voltage accelerated D^+ into the palladium target. During the 5 min. "off" periods, the sheath voltage was turned off, effectively stopping the D^+ ions from being implanted into the palladium target. The highest neutron production rate during this experiment was 188(2) n/s.

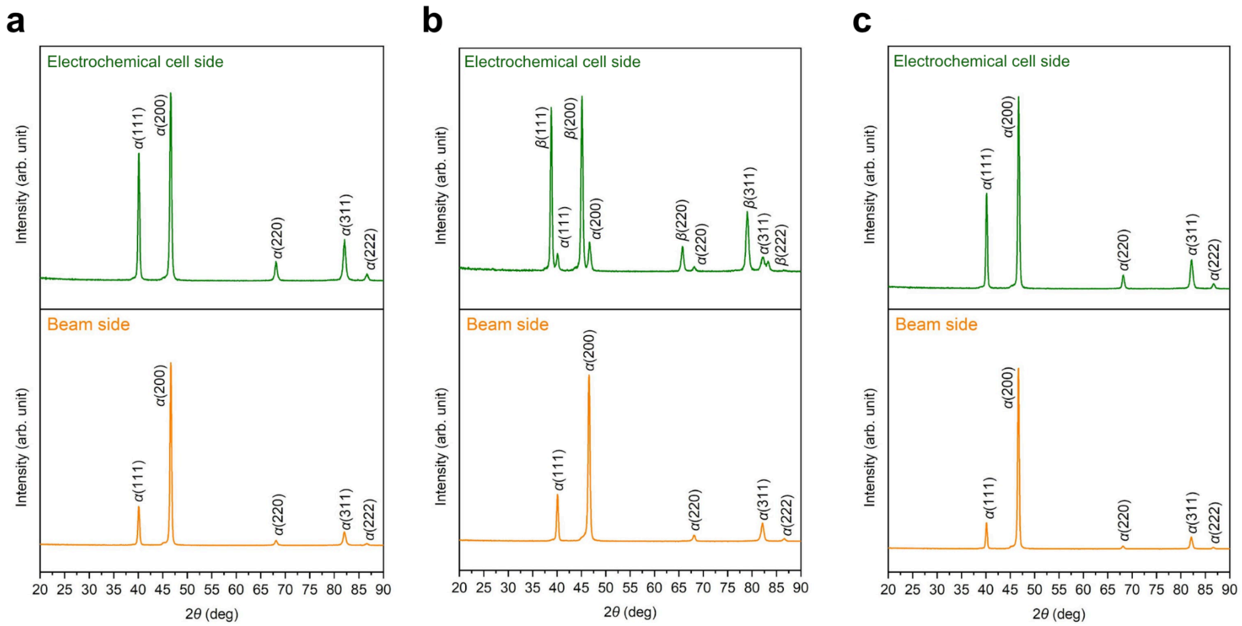

Supplementary Fig. 8: XRD spectra of a sample Pd target. **a**, XRD spectra of a Pd target prior to the fusion experiment. **b**, XRD spectra of a Pd target after the fusion experiment. **c**, XRD spectra of a Pd target after annealing. The fusion experiment included beam loading for 60 min with a sheath voltage of −30 kV and a plasma current of 0.5 mA and electrochemical loading for 60 min with a constant current of 200 mA across the electrochemical cell. The target was annealed at 400 °C for one hour at 10^{-5} Torr. XRD spectra were taken on both sides of Pd targets; the side exposed to the electrolyte in the electrochemical cell (denoted as "electrochemical cell side") and the other exposed to the D^+ beam in the vacuum chamber (denoted as "beam side").

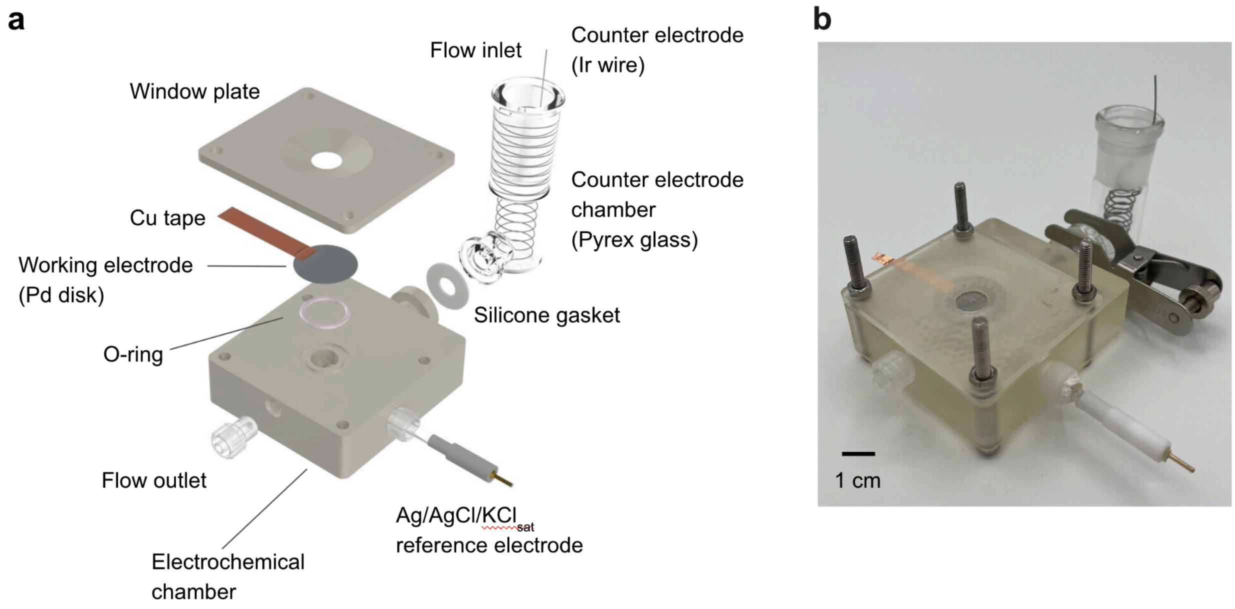

Supplementary Fig. 9: Electrochemical cell for *in situ* XRD experiments. a, CAD illustration of the 3D printed electrochemical cell for *in situ* XRD measurement. **b**, Photograph of the assembled electrochemical cell for *in situ* XRD measurement. A Pd target was sandwiched between the electrochemical chamber and a window plate. A strip of a Cu tape was attached to the Pd target as the electrical contact. The interface between the Pd target and the electrochemical cell was sealed using a Viton fluoroelastomer O-ring, exposing 1.5 cm^2 of the Pd target to the electrolyte, the same area as in the Thunderbird Reactor. The electrochemical chamber, Pd target, and window plate were clamped together using four M4 stainless steel screws. A counter electrode chamber made of pyrex glass was attached to the electrochemical cell using a stainless clamp and a silicone gasket for sealing. A 25 cm long Ir wire (0.5 mm, 99.95%) was formed into a screw shape and used as the counter electrode. A Ag/AgCl/KCl$_{sat}$ reference electrode was inserted near the Pd target through a hole in the electrochemical chamber. The electrolyte was circulated by using a Kamoer LLS Plus V2 peristaltic pump at a flow rate of 100 mL/min through the electrochemical cell.

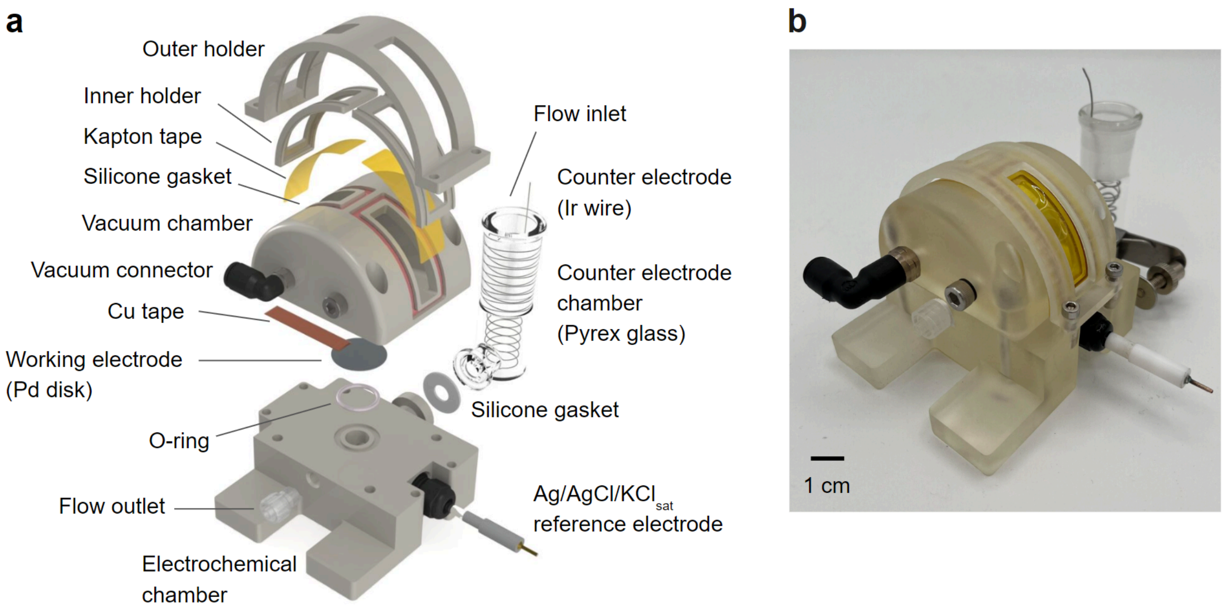

Supplementary Fig. 10: Electrochemical cell for *in situ* XRD experiments in vacuum. a, CAD illustration of the 3D printed electrochemical cell for *in situ* XRD measurement in vacuum. **b**, Photograph of the assembled electrochemical cell for *in situ* XRD measurement. A Pd target was sandwiched between the electrochemical chamber and a vacuum chamber. The vacuum chamber was sealed with semicircular-shaped frames that hold 25.4 μm-thick Kapton tapes as an X-ray transparent window. The vacuum chamber was connected to an Edwards E2M5 rotary pump through a vacuum connector and a PTFE tube to achieve 1.2×10^{-2} Torr. A strip of a Cu tape was attached to the Pd target as the electrical contact. The interfaces between the Pd target and the electrochemical and vacuum chambers were sealed using a Viton fluoroelastomer O-ring. 1.5 cm^2 of the Pd target, the same area as in the Thunderbird Reactor, was exposed to the electrolyte. The electrochemical chamber, Pd target, and vacuum chamber were clamped together using four M4 stainless steel screws. A counter electrode chamber made of pyrex glass was attached to the electrochemical cell using a stainless clamp and a silicone gasket for sealing. A 25 cm long Ir wire (0.5 mm, 99.95%) was formed into a screw shape and used as the counter electrode. A Ag/AgCl/KCl_{sat} reference electrode was inserted near the Pd target through a hole in the electrochemical chamber. The electrolyte was circulated by using a Kamoer LLS Plus V2 peristaltic pump at a flow rate of 100 mL/min through the electrochemical cell.

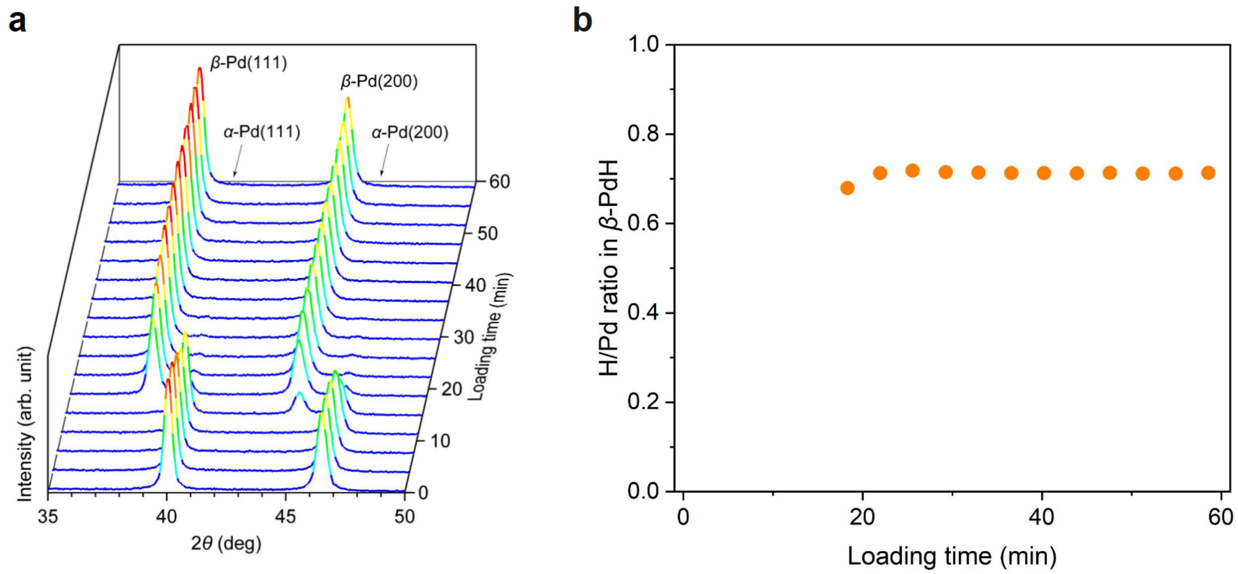

Supplementary Fig. 11: *In situ* XRD experiments for electrochemical loading cycle. a, 3D perspective view of XRD patterns of a Pd target as a function of electrochemical loading time. The Pd target was electrochemically loaded with hydrogen sourced from water electrolysis in 2 M K_2CO_3 in H_2O with a constant current of 200 mA for 60 min. Throughout this duration, XRD measurements were conducted repeatedly for $2\theta = 35$–50° at a scan rate of 5°/min. **b,** H/Pd ratio calculated from the lattice constant of the β-Pd(111) peak[26] as a function of loading time.

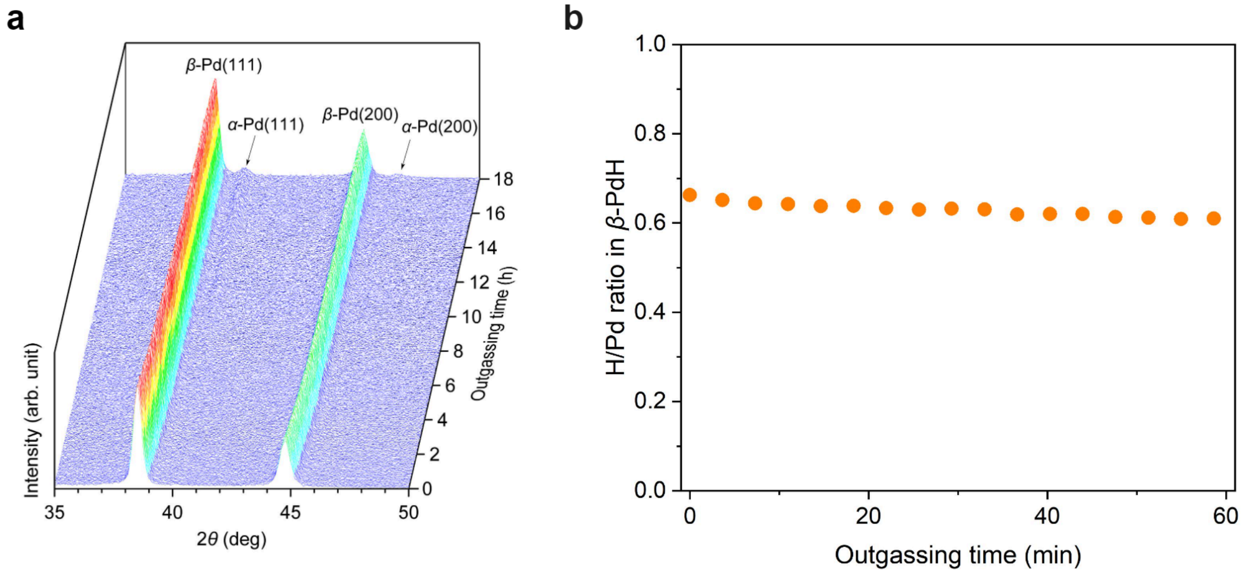

Supplementary Fig. 12: *In situ* XRD experiments for a natural outgassing cycle. a, 3D perspective view of XRD patterns of a Pd target as a function of outgassing time. The Pd target was first electrochemically loaded with hydrogen sourced from water electrolysis in 2 M K_2CO_3 in H_2O at a constant current of 200 mA for 60 min and then kept at its open circuit potential for 18 h. Throughout this duration, XRD measurements were conducted repeatedly for 2θ = 35–50° at a scan rate of 5°/min. **b**, H/Pd ratio calculated from the lattice constant of the *β*-Pd(111) peak[26] as a function of time for the initial 60 min of the outgassing cycle.

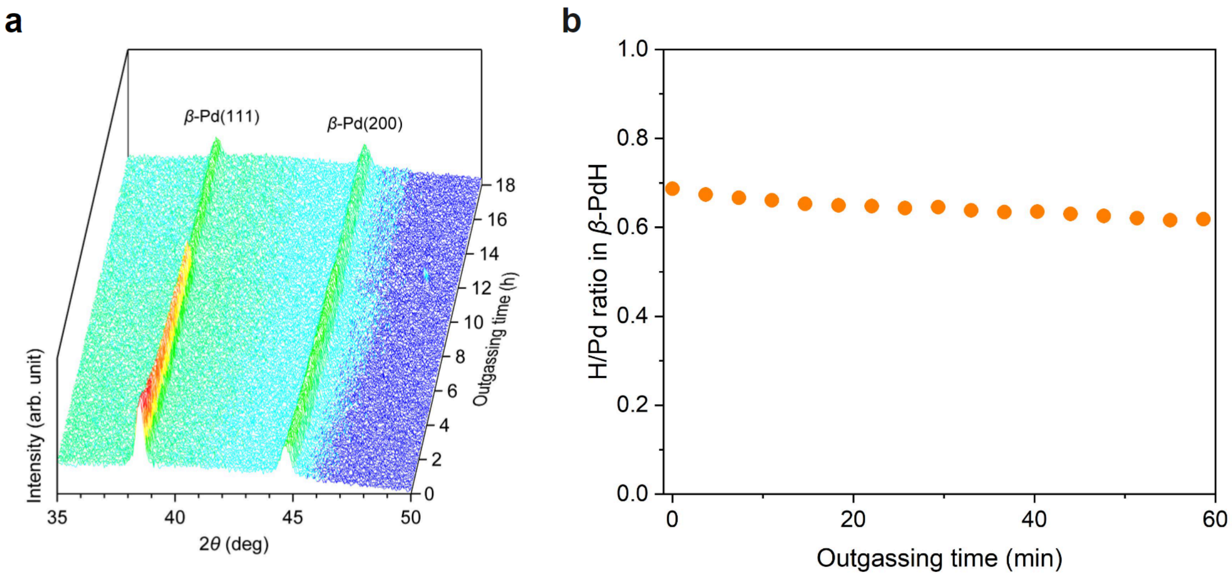

Supplementary Fig. 13: *In situ* XRD experiments for a vacuum cycle. a, 3D perspective view of XRD patterns of a Pd target as a function of outgassing time. The Pd target was first electrochemically loaded with hydrogen sourced from water electrolysis in 2 M K_2CO_3 in H_2O at a constant current of 200 mA for 60 min and then kept at its open circuit potential for 18 h. Throughout this duration, XRD measurements were conducted repeatedly for $2\theta = 35–50°$ at a scan rate of 5°/min. The cell was left under a vacuum of 1.2×10^{-2} Torr. **b**, H/Pd ratio calculated from the lattice constant of the *β*-Pd(111) peak[26] as a function of time for the initial 60 min of the outgassing cycle.

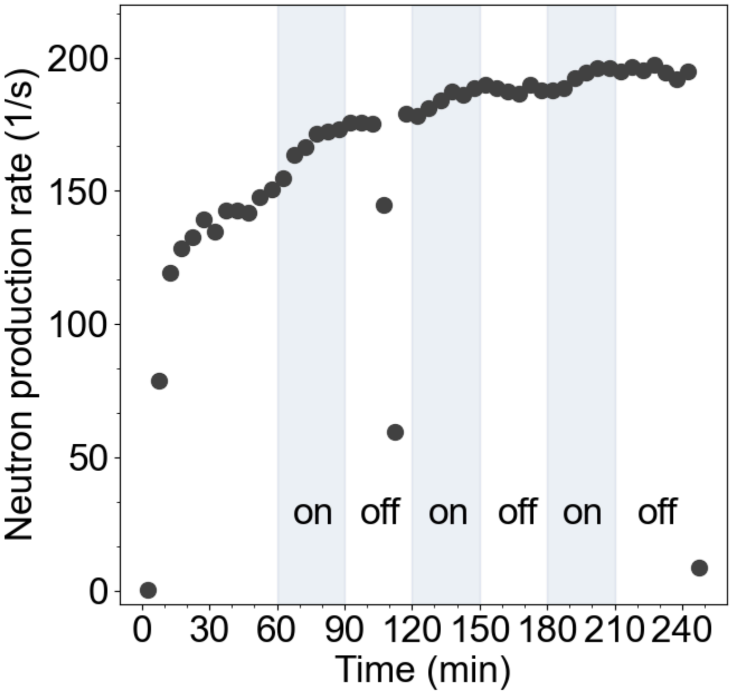

Supplementary Fig. 14: Effect of power cycling the electrochemical cell. Neutron production rates observed when the electrochemical cell was cycled on and off. The first 60 minutes are the beam loading period, and after reaching saturation, the electrochemical cell on/off cycle begins. During the 30 min 'on' periods, the deuterium was electrochemically loaded into the Pd target at a current of 200 mA. During the 30 min 'off' periods, electrochemical loading of deuterium into the Pd target was stopped. The neutron production rate increased with time while the electrochemical cell was 'on', and stopped increasing when the electrochemical cell was 'off'.

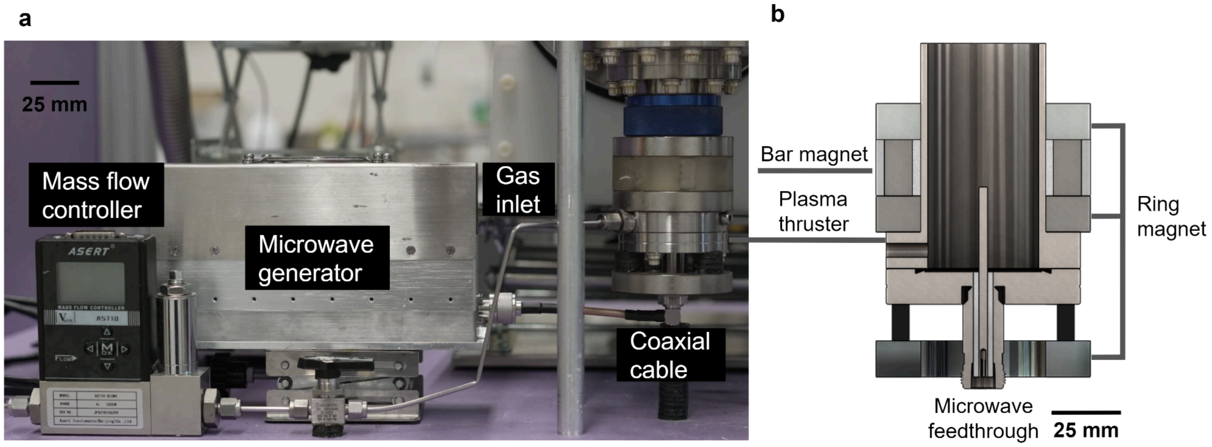

Supplementary Fig. 15: The plasma thruster of the Thunderbird Reactor. a, Photograph of the plasma thruster setup, showing the individual components required to operate the plasma thruster. **b**, CAD illustration of the cross-section of the plasma thruster.

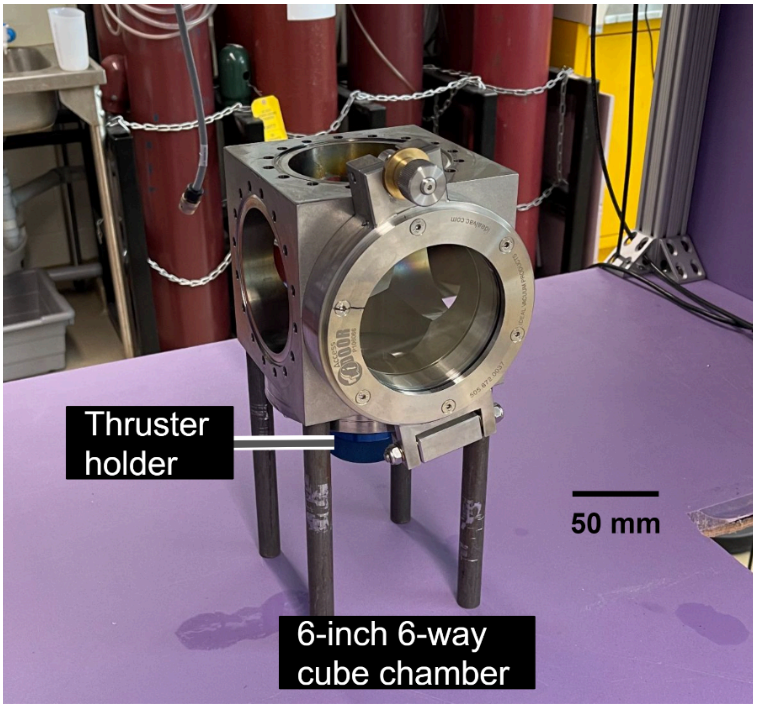

Supplementary Fig. 16: The vacuum chamber of the Thunderbird Reactor. A 6-inch, 6-way standard CF flange cube is at the center of the reactor. Its primary function is to physically connect the electrochemical cell and the plasma thruster while providing an appropriate vacuum environment for the operation of the plasma thruster and plasma immersion ion implantation (PIII).

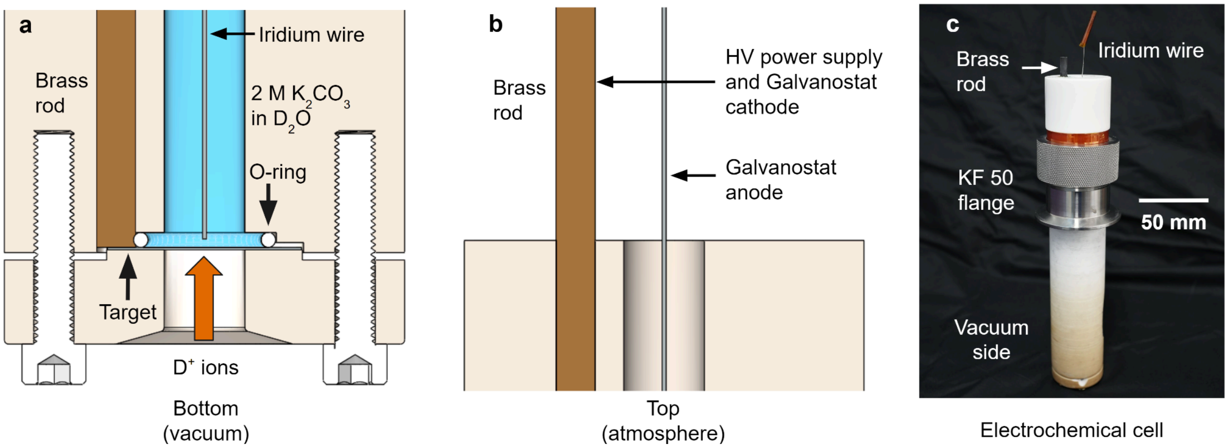

Supplementary Fig. 17: The Thunderbird Reactor electrochemical cell. a, Cross sectional schematic of the bottom of the electrochemical cell. **b,** Cross sectional schematic of the top of the electrochemical cell. **c,** The electrochemical cell is connected to the vacuum chamber via a KF 50 flange. The electrochemical cell is designed to separate the vacuum side and the atmospheric pressure side, and is used to bridge the electrochemical reaction and the nuclear fusion reaction. The vacuum side of the Pd target is bombarded by 30 keV D^+ ions, which is where the nuclear fusion reaction occurs.

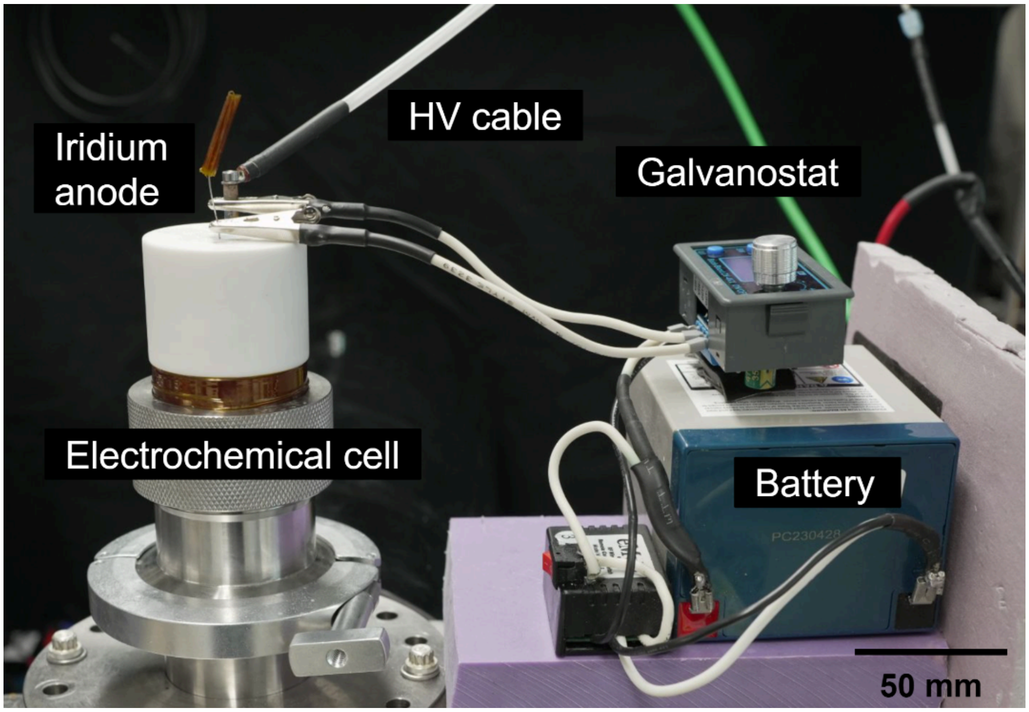

Supplementary Fig. 18: Electrochemical cell components in the Thunderbird Reactor. The palladium target is connected to the high-voltage power supply and the cathode of the galvanostat through a brass rod, while the iridium wire is connected to the anode of the galvanostat. The entire galvanostat operates at the potential 12 V. To ensure safe operation, a battery powers the galvanostat, and a remote control is used to trigger it.

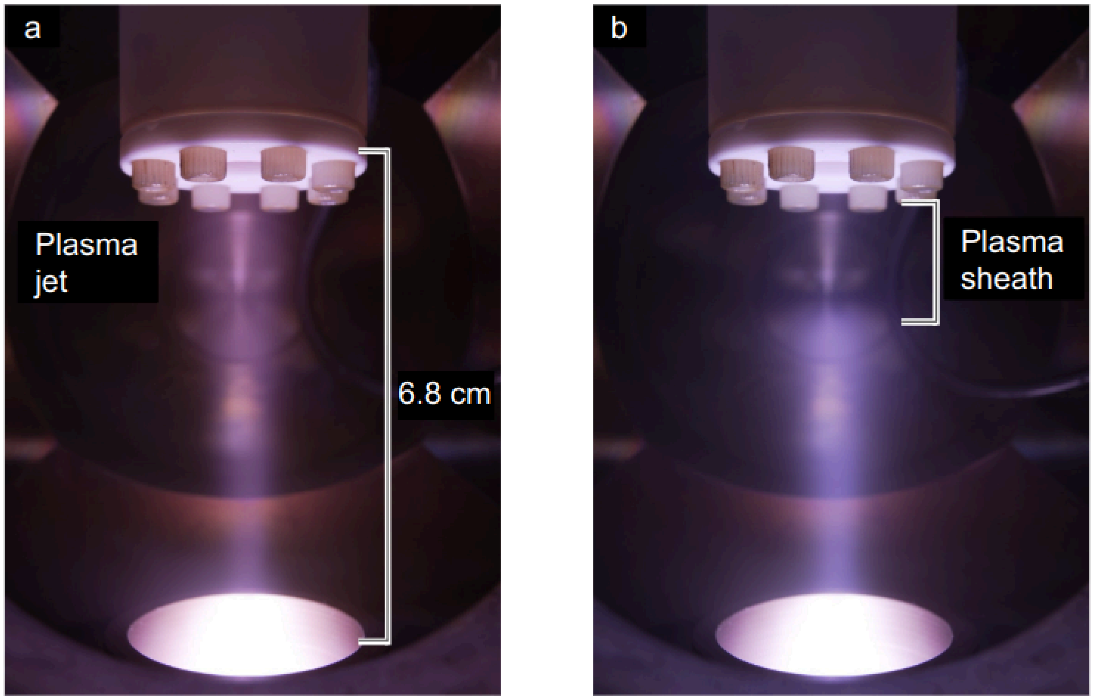

Supplementary Fig. 19: Photographs of the plasma in the vacuum chamber. a, The deuterium plasma jet generated by the plasma thruster engulfs the target material, but the nuclear fusion experiment has not yet started. **b,** When a negative high voltage is applied to the target, a plasma sheath is generated. Deuterium ions are then accelerated by the sheath voltage and injected into the target, initiating nuclear fusion reactions.

References

1. Schirber, J. E. & Morosin, B. Lattice constants of \beta-PdH$_x$ and \beta-PdD$_x$ with x near 1.0. *Phys. Rev. B Condens. Matter* **12**, 117–118 (1975).
2. Knoll, G. F. *Radiation Detection and Measurement*. (John Wiley & Sons, 2000).
3. Paff, M. G., Clarke, S. D. & Pozzi, S. A. Organic liquid scintillation detector shape and volume impact on radiation portal monitors. *Nucl. Instrum. Methods Phys. Res. A* **825**, 31–39 (2016).
4. Marquardt, N. Introduction to the principles of vacuum physics. *https://inspirehep.net › literaturehttps://inspirehep.net › literature* (1999).
5. Kentish, S. E., Scholes, C. A. & Stevens, G. W. Carbon Dioxide Separation through Polymeric Membrane Systems for Flue Gas Applications. *Recent Patents on Chemical Engineering* **1**, 52–66 (2008).
6. Tiesinga, E., Mohr, P. J., Newell, D. B. & Taylor, B. N. CODATA Recommended Values of the Fundamental Physical Constants: 2018. *J. Phys. Chem. Ref. Data* **50**, 033105 (2021).
7. *CoMPASS User Manual*. (2024).
8. Norsworthy, M. A. *et al.* Light output response of EJ-309 liquid organic scintillator to 2.86–3.95 MeV carbon recoil ions due to neutron elastic and inelastic scatter. *Nucl. Instrum. Methods Phys. Res. A* **884**, 82–91 (2018).
9. Enqvist, A., Lawrence, C. C., Wieger, B. M., Pozzi, S. A. & Massey, T. N. Neutron light output response and resolution functions in EJ-309 liquid scintillation detectors. *Nucl. Instrum. Methods Phys. Res. A* **715**, 79–86 (2013).
10. Safari, M. J. Differentiation method for Compton edge characterization in organic scin- tillation detectors. *Radiation Physics & Engineering* **1**, 9–16 (2020).
11. Chen, J. 40K. *Nucl. Data Sheets* **140**, (2017).
12. Kim, C., Yeom, J.-Y. & Kim, G. Digital n-γ Pulse Shape Discrimination in Organic Scintillators with a High-Speed Digitizer. *J. Radiat. Prot. Res* **44**, 53–63 (2019).
13. Brooks, F. D. DEVELOPMENT OF ORGANIC SCINTILLATORS. *NUCLEAR INSTRUMENTS AND METHODS* **162**, 477–505 (1979).
14. Nakhostin, M. *Signal Processing for Radiation Detectors*. (John Wiley & Sons, 2017).
15. Zaitseva, N. *et al.* Plastic scintillators with efficient neutron/gamma pulse shape discrimination. *Nucl. Instrum. Methods Phys. Res. A* **668**, 88–93 (2012).

16. Baramsai, B., Park, B., Becks, M. D., Chait, A. & Hendricks, R. Fast neutron spectroscopy with organic scintillation detectors in a high-radiation environment. *NASA* (2020).
17. Bai, H. *et al.* Calibration of an EJ309 liquid scintillator using an AmBe neutron source. *Nucl. Instrum. Methods Phys. Res. A* **863**, 47–54 (2017).
18. *MCNP User's Manual*. (2018).
19. Eriksson et al., J. Calculating fusion neutron energy spectra from arbitrary reactant distributions. (2015).
20. Bai, H. *et al.* Simulation of the neutron response matrix of an EJ309 liquid scintillator. *Nucl. Instrum. Methods Phys. Res. A* **886**, 109–118 (2018).
21. Andrews, M. T., Bates, C. R., Pinilla, M. I., McKigney, E. A. & Sood, A. Development of Validated Detector Models with MCNP® and DRiFT. in *2017 IEEE Nuclear Science Symposium and Medical Imaging Conference (NSS/MIC)* 1–3 (IEEE, 2017).
22. Holleck, G. L. Diffusion and solubility of hydrogen in palladium and palladium--silver alloys. *J. Phys. Chem.* **74**, 503–511 (1970).
23. Candler, R. N. Hopcroft, M. A Kim, B. Park, W-.T. Melamund, R. Agarwal, M. Yama, G. Partridge, A. Lutz, M. Kenny, T. W. Long-term and accelerated life testing of a novel single-waver vacuum encapsulation for MEMS resonators. *Journal of Microelectromechanical Systems* **15**, 1446–1456 (2006).
24. Santandrea, R. & Behrens, R. A review of the thermodynamics and phase relationships in the palladium-hydrogen, palladium-deuterium and palladium-tritium systems. *High Temp. Mater. Processes* **7**, 149–170 (1986).
25. Lässer, R. Isotope dependence of phase boundaries in the PdH, PdD, and PdT systems. *J. Phys. Chem. Solids* **46**, 33–37 (1985).
26. Benck, J. D., Jackson, A., Young, D., Rettenwander, D. & Chiang, Y.-M. Producing High Concentrations of Hydrogen in Palladium via Electrochemical Insertion from Aqueous and Solid Electrolytes. *Chem. Mater.* **31**, 4234–4245 (2019).